

2-dimensional ion velocity distributions measured by laser-induced fluorescence above a radio-frequency biased silicon wafer

Nathaniel B. Moore,^{1,a)} Walter Gekelman,^{1,b)} Patrick Pribyl,^{1,c)} Yiting Zhang,^{2,d)} and Mark J. Kushner^{2,e)}

¹Department of Physics and Astronomy, University of California, Los Angeles, California 90095, USA

²Department of Electrical Engineering and Computer Science, University of Michigan, 1301 Beal Ave., Ann Arbor, Michigan 48109-2122, USA

(Received 2 April 2013; accepted 3 July 2013; published online 8 August 2013)

The dynamics of ions traversing sheaths in low temperature plasmas are important to the formation of the ion energy distribution incident onto surfaces during microelectronics fabrication. Ion dynamics have been measured using laser-induced fluorescence (LIF) in the sheath above a 30 cm diameter, 2.2 MHz-biased silicon wafer in a commercial inductively coupled plasma processing reactor. The velocity distribution of argon ions was measured at thousands of positions above and radially along the surface of the wafer by utilizing a planar laser sheet from a pulsed, tunable dye laser. Velocities were measured both parallel and perpendicular to the wafer over an energy range of 0.4–600 eV. The resulting fluorescence was recorded using a fast CCD camera, which provided resolution of 0.4 mm in space and 30 ns in time. Data were taken at eight different phases during the 2.2 MHz cycle. The ion velocity distributions (IVDs) in the sheath were found to be spatially non-uniform near the edge of the wafer and phase-dependent as a function of height. Several cm above the wafer the IVD is Maxwellian and independent of phase. Experimental results were compared with simulations. The experimental time-averaged ion energy distribution function as a function of height compare favorably with results from the computer model. © 2013 AIP Publishing LLC. [<http://dx.doi.org/10.1063/1.4817275>]

I. INTRODUCTION

The energy and angle of impact of ions on the surface of wafers during plasma etching processes are critical parameters for the fabrication of microelectronic devices.¹ Control of these parameters allows for finer control in etch rate and etch anisotropy.¹ The region of the plasma where ions experience the majority of their acceleration—the sheath—is difficult to investigate due to its being thin, typically less than a few mm, and being transient due to the radio frequency (rf) biasing that is typically used. Electrical probes are difficult to use in the sheath as the probe and sheath are comparable in size. A probe creates its own sheath which could perturb the characteristics that are being measured. Computer models^{2–9} and analytic investigations^{10–17} have provided insights to the dynamics of ions while being accelerated through sheaths.

Control of ion energy distributions (IEDs) [or ion velocity distributions (IVDs)] in the context of plasma etching in microelectronics fabrication has made impressive progress. A variety of techniques have been developed which utilize multiple rf frequencies,^{5–7,18} non-sinusoidal waveforms⁸ and pulsed power.^{9,19} Control of IEDs in many of these techniques is based on the time for ions to cross the sheath, τ_{ion} , compared to the rf period, τ_{rf} . Defining $\omega_{rf} = 2\pi/\tau_{rf}$ and $\omega_{ion} = 2\pi/\tau_{ion}$, the ratio of these two frequencies, ω_{rf}/ω_{ion} ,

is an important parameter controlling ion dynamics in the sheath. For low frequency biases ($\omega_{rf}/\omega_{ion} \ll 1$), the transit of ions across the sheath during the rf period appears to be an ensemble of DC sheaths—the ion dynamics are essentially determined by the rf phase and voltage at which the ions enter the sheath.⁹ In this regime, the time-averaged IED is bimodal.² As the rf bias frequency is increased, the separation between peaks of the bimodal distribution, ΔE_i , decreases. At high frequencies ($\omega_{rf}/\omega_{ion} \gg 1$) $\Delta E_i \rightarrow 0$ and the IED converges to a single peak at \bar{V}_s , corresponding to the average sheath potential.^{9,13} The intermediate regime ($\omega_{rf}/\omega_{ion} \approx 1$) has been more difficult to analytically model as the ion dynamics heavily depend on both the rf phase at which the ions enter the sheath and how many RF periods the ion experiences in crossing the sheath.^{12–15} As a result, most models addressing this regime have been numerical.^{2–9,13,14}

IEDs striking the substrate in plasma processing reactors are typically measured using energy resolved mass spectrometers or gridded ion energy analyzers. The first of these experiments measured the ion energy distribution function at a grounded electrode with a small sampling hole.^{20,21} Subsequent experiments were able to take similar measurements at an rf-powered electrode.^{22–27} The time-averaged, single position energy distribution function measurements from all of these experiments tended to confirm the predicted feature of two peaks separated in energy.

The measurements of IEDs and IVDs to date have typically emphasized the characteristics of the ions striking the substrate. Several studies have investigated IVDs in the presheath. These have been done over unbiased surfaces,^{28–31} dc biased surfaces,^{32,33} and in rf sheaths.³⁴ Claire *et al.*³⁰

^{a)}moore@physics.ucla.edu

^{b)}gekelman@physics.ucla.edu

^{c)}Pribyl@physics.ucla.edu

^{d)}yitingz@umich.edu

^{e)}mjkush@umich.edu

measured both longitudinal and transverse IVDs in both the presheath and sheath above a floating plate in a multipolar dc discharge. Measurements along a line extending from the presheath to the sheath above an rf biased silicon wafer were done by Jacobs *et al.*³⁴ The work presented in this paper is an extension of this experiment. In this paper, we describe measurements of IVDs using laser-induced-fluorescence (LIF) in a commercial inductively coupled plasma (ICP) sustained in an Ar/O₂ gas mixture of a few mTorr pressure with an rf bias on the substrate. IVDs are measured from the bulk plasma, into the presheath and through the sheath. The frequency of the applied bias, 2.2 MHz, places this experiment in the intermediate ω_{rf}/ω_{ion} regime ($\omega_{rf}/\omega_{ion} \approx 3.4$). The LIF technique and experiment are discussed in Sec. II following by a discussion of results for IVDs in Sec. III. Corroborating results from numerical simulations are presented in Sec. IV, followed by our concluding remarks in Sec. V.

II. DESCRIPTION OF THE LIF TECHNIQUE AND EXPERIMENT

LIF is a non-invasive plasma diagnostic that has been used to measure various ion and plasma properties.^{35–37} The technique allows for multiple spatial positions to be simultaneously probed with a temporal resolution determined by the width of the laser pulse (typically on the order 10 ns) and the lifetime of the excited state. In the context of low pressure plasmas for materials processing, the technique has been used to measure ion densities, drift velocities, and energy distribution functions in dc and rf sheaths.^{28–34,38–42} The electric field inside an rf sheath has also been measured by using a two-step process called LIF-dip in which the field is calculated from the Stark shifted fluorescence from ions.^{43,44}

Our implementation of the LIF technique uses the $3d^2G_{9/2} \rightarrow 4p^1F_{7/2}$ transition in argon. A metastable ion state (State 1, $3d^2G_{9/2}$) absorbs a laser photon with an energy matching a specific transition to a short-lived excited state (State 2, $4p^1F_{7/2}$). Depending on the metastable state being probed, this excited state can radiatively relax to the original state or to a different state (State 3, $4s^1D_{5/2}$). This second transition will then emit a fluorescent photon at a different energy from the pump photon whose frequency can be detected, for example, with a photomultiplier tube or CCD camera. This is the LIF signal. The strength of the LIF signal is proportional to the density of State 1, which is representative of the ground state density.⁴¹ This method can be used to obtain IVDs in the plasma. The frequency of the incident photon in the frame of reference of the metastable atom in the State 1 \rightarrow State 2 transition will depend on the relative velocity of the atom with respect to the direction of the laser beam due to Doppler shifting. By probing the plasma with a range of wavelengths (such as from a tunable dye laser), one can obtain the ion velocity distribution functions from the LIF signal,

$$2\pi\Delta\nu = 2\pi(\nu_L - \nu_0) = \vec{v} \cdot \vec{k} = v_{\parallel}k, \quad (1)$$

where ν_L is the laser probing frequency, ν_0 is the center line frequency of the Doppler shifted transition, \vec{v} is the ion velocity, and \vec{k} is the laser wavevector. The State 1 \rightarrow State 2

transition in this implementation is pumped by a 611.492 nm photon and the measured State 2 \rightarrow State 3 transition emits a 461 nm photon. A narrow band-pass filter is used to mask out the pump beam as well as other plasma line radiation. This is necessary because the 461 nm light has a much lower intensity.

The Doppler shift is not the only mechanism contributing to the broadening the LIF signal under these conditions. The lineshape is also subject to power broadening.⁴⁰ As there are only a finite number of metastable states with velocities corresponding to the center of the beam profile, all of the metastable states will be excited from State 1 \rightarrow State 2 when a threshold laser power is exceeded. The LIF signal then saturates and increasing power does not result in an increased signal, at least from these atoms. However, the incident laser radiation is not strictly monoenergetic as even a narrow banded laser has a finite spectral width. Photons from the wings of the incident beam induce fluorescence from a population of atoms moving at increasingly divergent velocities. As a result, the apparent velocity distribution can be broadened depending on the incident power.

Power broadening can be avoided by using a lower laser power, but in our case doing so significantly reduces the signal-to-noise ratio of the measurement. The amount of averaging that would be needed to reduce the noise to a reasonable level would unacceptably increase the time for taking a complete data set. For this reason, except for calibration, a relatively high laser power was intentionally used ($\approx 1 \text{ kW/cm}^2$ entering the reactor per laser pulse). The measured LIF signal must then be deconvolved to extract the unbroadened IVD. In general, the measured signal is a convolution of the true signal with the broadening mechanism,

$$i(v_z) = (s \otimes o)(v_z) = \int_{-\infty}^{\infty} s(v_z - v'_z) o(v'_z) dv'_z, \quad (2)$$

where $i(v_z)$ is the image function (the measured data, in this case), $s(v_z)$ is the spread function (from power broadening), and $o(v_z)$ is the object function (the true IVD). To obtain the true IVD, the measured signal must be deconvolved with the spread function.

A maximum entropy algorithm was used for deconvolution.⁴⁵ To obtain the spread function, first a low intensity scan was performed to measure an unbroadened IVD in the bulk of the plasma where the average velocity is approximately zero. A spread function is computed by deconvolving a broadened distribution function from a high intensity scan with the unbroadened distribution function. This spread function is then used in all subsequent scans to obtain the true IVDs. This technique will ultimately overestimate the temperature of the cold, background ions, but not the high energy tail that is of interest in plasma processing.

The ICP reactor used in the experiment, schematically shown in Fig. 1(a), is a modified commercial plasma etch tool provided by the Intevac Corp. The chamber is approximately cylindrical with a diameter of 50 cm and height of 40 cm. Ports were added to the sides and top of the chamber to allow access for diagnostics. The ICP is produced by a 500 W, 440 kHz solenoidal antenna surrounding a ceramic

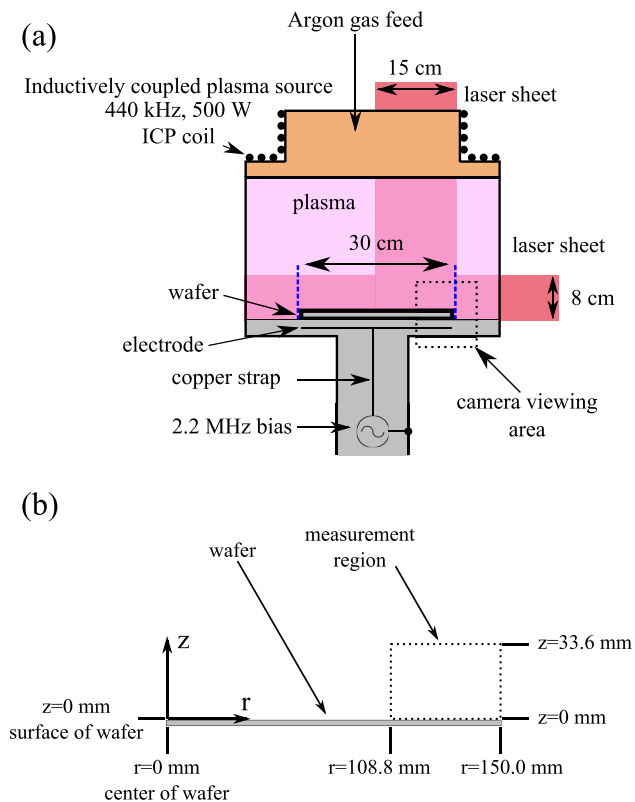


FIG. 1. Schematics of the experimental apparatus (a) plasma chamber. (b) The coordinates and region above the wafer used for the analysis.

cap to the plasma chamber. The ceramic cap sits on the aluminum chamber. For this experiment, gas entered the chamber through six symmetrically spaced feed nozzles in an aluminum plate on the top of the chamber and was exhausted by a turbomolecular pump at the bottom of the chamber. This plate included a window and replaced the original showerhead. The feedstock gas was $\text{Ar}/\text{O}_2 = 80/20$ at a pressure of 0.5 mTorr. The fill pressure was necessarily lower than that typically used in semiconductor processing (10–100 mTorr) as collisions with neutrals would begin quenching the metastable ions used in the LIF diagnostic at pressures as low as a few mTorr. Since operation of the plasma tool required a silicon wafer on the substrate, the small rate of sputtering Si atoms in pure argon plasmas eventually deposited on and covered the windows of the chamber, which would have required frequent cleaning of the chamber on times shorter than a typical diagnostic run. Oxygen was added to enable *in situ* cleaning of the windows.

The 30 cm diameter silicon wafer was electrostatically clamped to the chuck at the bottom of the chamber. The volume above the wafer in which measurements were taken is shown in Fig. 1(b). The 2.2 MHz rf bias was run with an 11% duty-cycle and pulsed frequency of 10 Hz delivered from the source to the electrode underneath the wafer via a copper strap after a fixed match network. This results in the rf bias being on for 11 ms with a 10 Hz repetition rate, with LIF measurements being made in the last 1 ms of the pulsed bias. This rf pulse length is sufficiently long that the IVDs at all frequencies of interest are in a quasi-steady state at the time that the LIF measurements are made. The bias current

and voltage were measured at the current strap. Impedance of the strap, wafer, and plasma were then used to estimate the applied rf voltage both at the chuck and at the surface of the wafer. The latter was approximately 600 V peak-to-peak. Taking into account the plasma potential and uncertainty in the voltage measurement, the maximum sheath potential drop was approximately 650 V. Data were taken at eight different phases of the rf cycle, as shown in Fig. 2.

Bulk plasma parameters were measured at 317 spatial locations in a plane 2 cm above the wafer using a Langmuir probe connected to an automated drive mechanism capable of positioning the probe in a 2D plane. For these probe measurements, the ICP source was pulsed and measurements were taken $50 \mu\text{s}$ and later following the shutdown of the ICP source. This significantly reduced rf noise introduced from the ICP source and obviated the need for an rf compensated probe. The electron temperature, T_e , and ion density, n_i , were calculated at $100 \mu\text{s}$ intervals from the I–V traces. At $100 \mu\text{s}$, in the middle of the wafer, T_e was measured to be $\approx 1.7 \text{ eV}$ and $n_i \approx 2 \times 10^{10} \text{ cm}^{-3}$. (See Fig. 3.) Although T_e may be somewhat lower than during the ICP power on stage, n_i likely closely approximates that during the ICP power on stage.

A tunable dye laser probed the 611.49 nm range needed for the LIF scheme used here. The dye laser was pumped by a Spectra Physics Quanta-Ray Nd:YAG laser that was frequency-doubled to 532 nm. The pump laser was pulsed at 10 Hz with each pulse having 10 ns duration and an energy of 450 mJ. The dye laser was a Sirah Cobra-Stretch with a Rhodamine B and Rhodamine 101 dye mixture which in turn generated 85 mJ pulses at wavelengths ranging from 611.350 nm to 611.650 nm. The laser wavelength was stepped at increments of 1 pm. The wavelength was calibrated using a HighFinesse meter, accurate to 0.5 pm (or, in units of ion velocity, to within approximately 0.3 km/s, or $3 \times 10^2 \text{ m/s}$). A pair of Glan-Thompson polarizers was placed after the dye laser in order to control the beam energy, and the beam was delivered to the reactor through a 1 mm fiber optic cable. The energy on the reactor side of the fiber was set to $250 \mu\text{J}$ per pulse for each experimental run.

Light exiting the fiber was collimated onto a plano-convex converging lens by an aspherical lens. The beam was

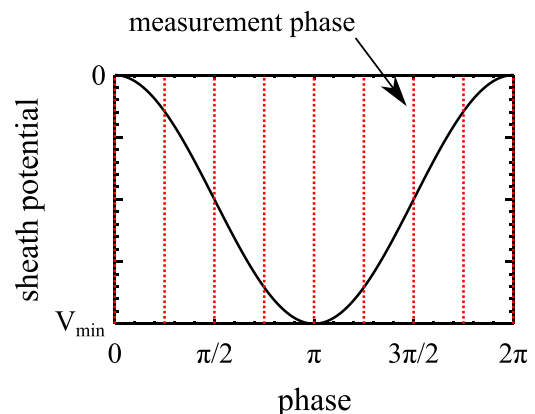


FIG. 2. Phase reference diagram. The vertical lines represent phases at which measurements were taken.

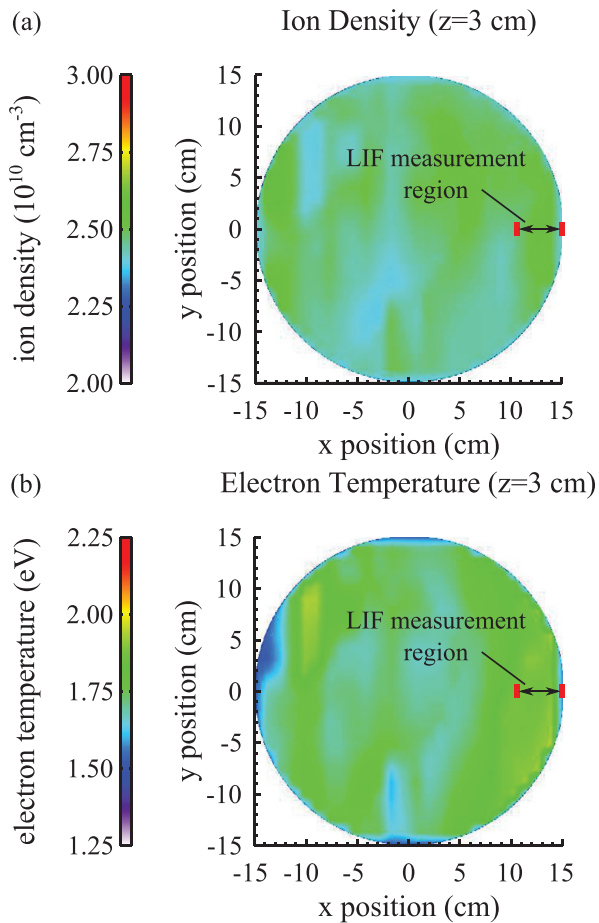


FIG. 3. Bulk plasma parameters 3 cm above the wafer ($100\ \mu\text{s}$ after ICP shutoff) measured using a Langmuir probe. (a) Electron temperature calculated from the exponential region of the measured I–V curve. (b) Ion density calculated from the ion saturation current and T_e .

passed through two cylindrical lenses to create a sheet of laser light. Spatial variation in laser intensity across the sheet was accounted for in the final measured signal. For IVD measurements perpendicular to the surface of the wafer, the planar laser sheet entered the chamber through a rectangular window located on top of the chamber. For IVD measurements parallel to the wafer's surface, the laser sheet entered through a circular window on the side of the chamber, centered on the surface of the wafer.

The LIF signal was recorded using a fast (30 ns exposure), 12 bit DiCam-Pro Intensified CCD camera. The axis of the camera was centered vertically along the top edge of the wafer and aligned to record images of the fluorescence above the outer 10 cm of the diameter of the wafer. The images were 1280 pixels wide by 1056 pixels tall and were averaged over 1000 shots. These images were then averaged over 2×2 pixel bins twice, once by the data acquisition software and once again before analysis, to give a final resolution of 320×256 pixels. An absolute spatial calibration was performed by imaging a $1\ \text{cm} \times 1\ \text{cm}$ gridded aluminum plate placed in the laser path inside the plasma chamber. After the pixel averaging, the final resolution was $0.4\ \text{mm} \times 0.4\ \text{mm}$ per pixel.

The timing sequence used for the experiment is schematically shown in Fig. 4. A photo-diode was used to

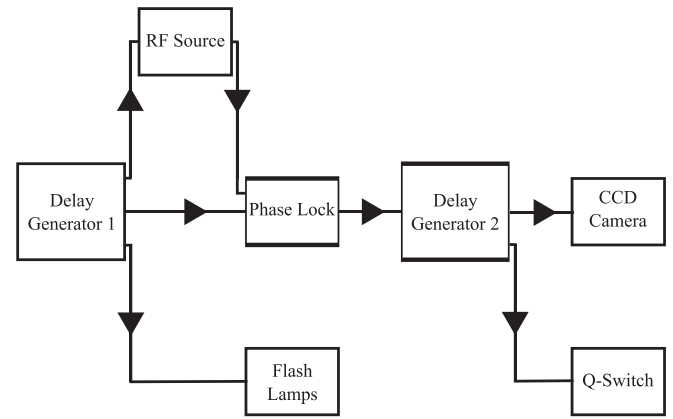


FIG. 4. Schematics of the timings. Two delay generators are used in the experiment. The first delay generators triggers first the RF source (11 ms pulse width) and then the phase lock and laser flash lamps after 10 ms (to allow the plasma response to the applied RF to stabilize). The phase lock receives a signal from a voltage divider on the copper strap leading up to the chuck and outputs a trigger for a second delay generator once the voltage waveform crosses zero. The second delay generator then triggers the CCD camera and the laser Q-switch. The Q-switch timing varies depending on the desired RF phase for LIF measurements.

measure laser light immediately before entering the plasma chamber. The signal from the photo-diode, along with adjustments to the delay between the phase lock and the Q-switch of the laser, was compared with the voltage waveform to calibrate the phase measurements. The pulse width of the laser and timing jitter combined were approximately 40 ns. This spread in time corresponds to a maximum uncertainty in the sampled bias voltage of 60 V. The base repetition rate of the entire experiment was set by the laser, which ran at 10 Hz. An average run which provided either a parallel or perpendicular component of the IVD at one phase and 82 000 spatial locations consisted of 1000 camera shot averages at 300 wavelength points, and required upwards of 10 h to complete. A typical complete run for all phases and both laser orientations required up to two weeks of continuous data acquisition.

III. ION VELOCITY DISTRIBUTIONS MEASURED BY LIF

A typical deconvolved vertical IED measured at various heights above the wafer when the rf phase of the bias is most negative ($\phi = \pi$) is shown in Fig. 5. Data corresponding to particles moving upward were ignored as it was not possible to distinguish between the LIF signal from actual particles moving in this direction and the signal from light reflected off the surface of the wafer. Data for heights less than 1.2 mm were also ignored as the signal was too small to be reliable due primarily to the decrease in ion density. Since the total ion flux is conserved, the ion density decreases as the velocity increases approaching the wafer surface. The deconvolved IED has a width larger than what would be expected from the bulk ion temperature. The width can be attributed in part to the deconvolution algorithm and in part to the aforementioned 60 V uncertainty in the sampled bias voltage.

For an unbiased wafer, the thickness of the sheath is estimated to be $s \approx 10 \lambda_D = 0.5\ \text{mm}$. The measured sheath

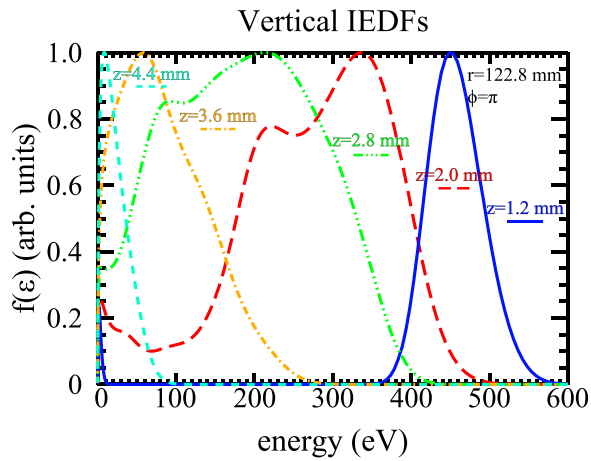


FIG. 5. Example vertical ion energy distribution function at multiple heights for the most negatively biased phase. IED widths larger than what would be expected from the bulk ion temperature can be attributed to a combination of the deconvolution algorithm and an uncertainty in the sampled bias voltage due to timing jitters and the laser pulse width.

thickness for the biased case was $s \approx 4.0$ mm at a radius on the wafer of $r = 105$ mm compared with a predicted value of 3.2 mm.⁹ The measured sheath thickness did not change significantly towards the edge of the wafer.

These sampled vertical IEDs show the emergence of high energy ions as the particles enter the sheath region. The distribution function in the plasma bulk is essentially Maxwellian, with the peak centered at $v_z = 0$. At 4 mm above the wafer, near the edge of the sheath, the peak begins to shift and widen. Close to the surface of the wafer at this phase, high energy (400–500 eV) ions dominate. However, a small Maxwellian peak corresponding to stationary ions remains. This would need to result from ionization or charge exchange near the surface of the wafer. Since the mean free path for collisions exceeds the sheath width, it is not clear what the mechanism for producing these low energy ions is, or whether they are an artifact of the measurement. The horizontal IED is shown in Fig. 6 at the same positions and phase. There is little variation in the horizontal IED at different heights other than the change in magnitude due to the

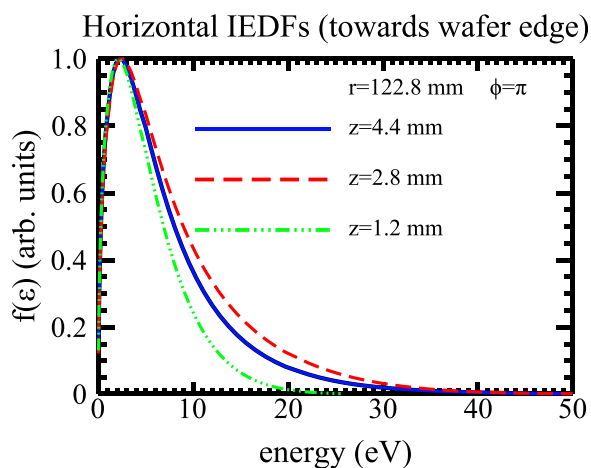


FIG. 6. Horizontal ion energy distribution function at multiple heights above the wafer for $\phi = \pi$.

decrease in ion density. The distribution function remains primarily Maxwellian with little acceleration of ions to large velocities parallel to the surface of the wafer.

Planar laser illumination allows comparison of distribution functions at multiple horizontal positions across the surface of the wafer. Vertical IEDs between mid-wafer and the wafer edge for two phases are shown in Figs. 7 and 8. For the phase when the bias is most negative ($\phi = \pi$), ions ($\epsilon > 10$ eV) are accelerated from the zero-net velocity distribution at a height of about 4 mm where the sheath starts. At mid-wafer (4 cm from the edge), the ions accelerate to an average energy of 450 eV with a maximum extent of roughly 500 eV about 1.2 mm above the surface of the wafer, which is the extent of our measurement. If the IED is linearly extrapolated to zero height (at the wafer surface), the estimated average energy is 600 eV and the maximum energy is about 650 eV. Ions at the edge of the wafer accelerate to approximately the same energies. For the phase having the least negative bias ($\phi = 0$), there was little variation between mid-wafer and the edge of the wafer as few fast ions were observed in either case. The radial dependence of the vertical IED at all heights is shown in Fig. 9.

Taking the average over all measured phases yields the time-averaged IEDs shown in Fig. 10 at a height of 2 mm.

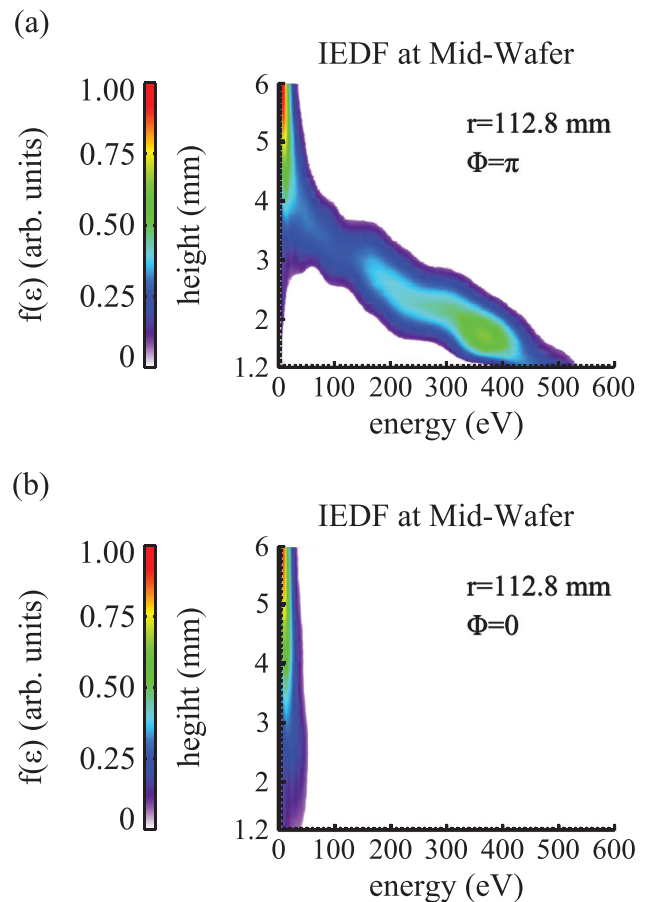


FIG. 7. Vertical IEDs at mid-wafer ($r = 112.8$ mm) for two different phases. (a) IED for $\phi = \pi$. Ions are accelerated from the thermal distribution prior to the presheath as the ions enter the sheath. The maximum energy reached by these ions at 1.2 mm, the lowest observation height, is approximately 500 eV. (b) IED for $\phi = 0$. For this phase, the distribution remains primarily Maxwellian through as the ion transit time is short compared to the rf cycle.

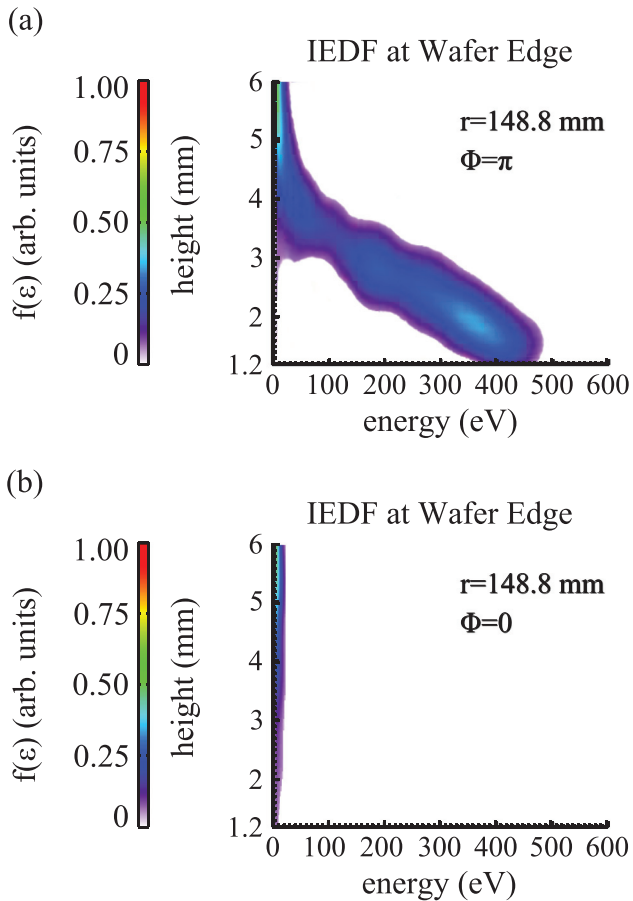


FIG. 8. Vertical IEDs at the edge of the wafer ($r = 148.8$ mm) for two different phases. (a) IED for $\phi = \pi$. Ions accelerate to energies comparable to those reached at mid-wafer. (b) IED for $\phi = 0$. The distribution remains essentially Maxwellian through the sheath.

Averages both at the edge of the wafer and at the middle of the wafer give the expected two-peak structure. While the overall shape and relative heights of the two peaks change with radial position, the energy separation ΔE_i at the edge and mid-wafer is the same, roughly 220 eV. This measurement is consistent with previous work performed in this reactor.³⁴

Calculated mean ion velocities ($\bar{v} = \frac{1}{n} \int v f(r, z, \phi, v) dv$) were compared at multiple phases of the rf bias and are shown in Fig. 11. These plots have the horizontal component of the velocity vector increased by a factor of 10 to emphasize the radial velocity. For $\phi = \pi$ (most negative bias), ions near the surface of the wafer have a highly directed velocity downward towards the wafer, with a maximum of $v_z = 1.2 \times 10^4$ m/s reached at $r = 110$ mm and $z = 2.0$ mm. Closer to the radial edge of the wafer, $r = 150$ mm, and higher above the surface of the wafer ($z > s$, the sheath thickness), the velocities have a larger perpendicular component. For the least negative bias, $\phi = 0$, the horizontal component of the velocity is much more significant compared to the strongly biased case, though the maximum velocity reached is much less ($v = 2.3 \times 10^3$ m/s).

The heat flux ($Q = M \int v^2 f(r, z, \phi, v) dv$) calculated from the IVDs varied significantly across the eight measured phases and horizontally across the wafer surface. Away from the edge of the wafer ($r = 112.8$ mm), the peak heat flux was

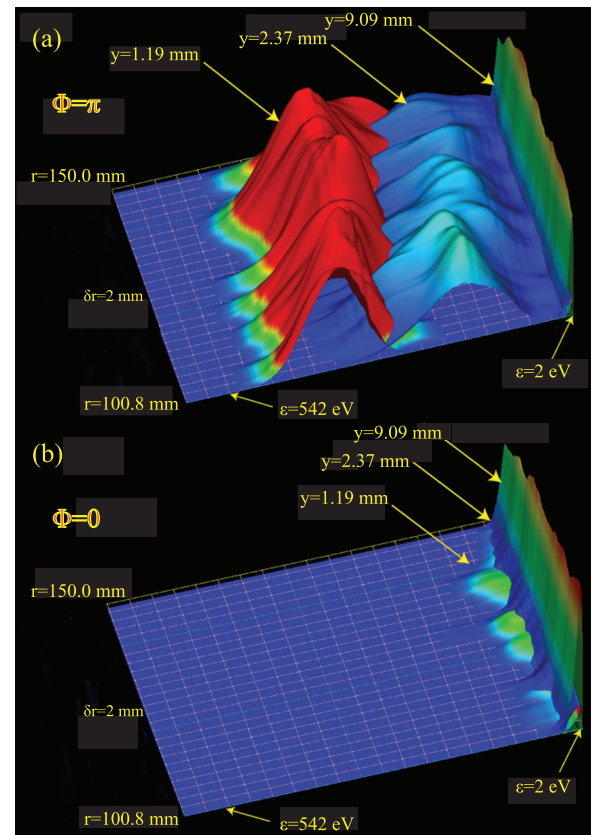


FIG. 9. The ion distribution functions as a function of energy and radial position at three heights above the wafer. (a) IED at $\phi = \pi$. At $z = 1.2$ mm, the IED peaks at approximately 500 eV. This peak remains relatively unchanged across several radial positions. (b) IED for $\phi = 0$. Few high energy ions are present at any height or radial position.

5.2 kW/m² at $\phi = \pi$, 2 mm above the surface, as shown in Fig. 12. At the edge of the wafer ($r = 146$ mm), the heat flux for this phase drops to 3.9 kW/m². For the intermediate phases, the drop in heat flux from mid-wafer to the wafer edge is also present. For example, at $\phi = 3\pi/2$, the heat flux decreases from 3.1 kW/m² to 1.9 kW/m². Heat fluxes for phases near the least negative bias were (expectedly) much less than the peak heat flux at all horizontal positions. If we extrapolate these powers to the surface of the wafer and average over the cycle, the heat flux due to ion transport is

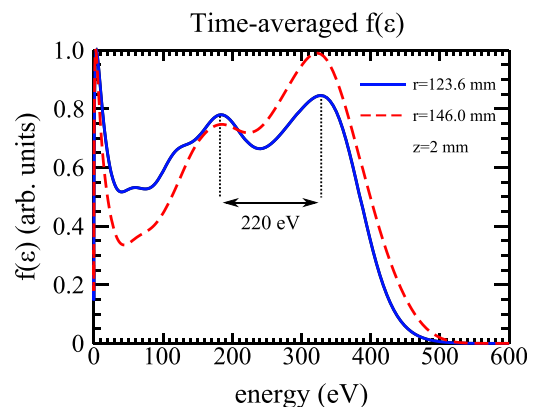


FIG. 10. Time-averaged ion energy distribution functions at the edge of the wafer and towards the center of the wafer. The energy peak separation is approximately 220 eV for both cases.

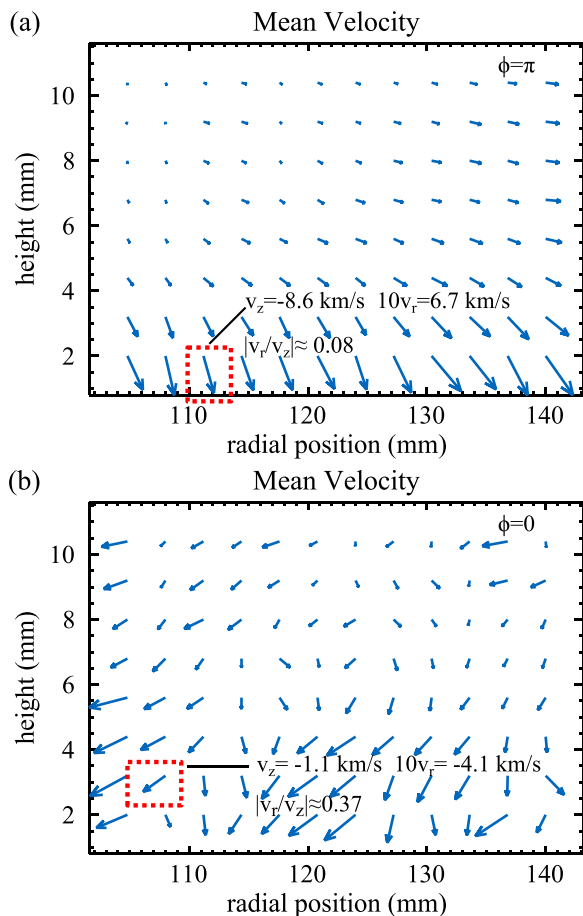


FIG. 11. Mean velocity vectors for two disparate phases. The radial component of velocity is multiplied by 10 to emphasize radial variations in the velocities. (a) Phase $\phi = \pi$. Towards the middle of the wafer, the velocities are dominantly downward towards the wafer. Closer to the edge of the wafer, the mean velocities have a larger radial contribution directed away from the center of the wafer. (b) Phase $\phi = 0$. For this phase, the radial component is a more significant part of the mean velocity.

approximately 300 W. The average power deposition at 2 MHz for the bias is 400 W, which confirms that the majority of the power deposited into the sheath is used in ion acceleration.

IV. ION VELOCITY DISTRIBUTIONS PREDICTED BY MODELING

The corroborating simulations were performed using the Hybrid Plasma Equipment Model (HPEM), described in detail in Refs. 46 and 47 and briefly discussed here. As a hybrid model, the HPEM has a hierarchical structure in which different modules address different physical processes. For this study, the Electron Magnetic Module (EMM), Electron Energy Transport Module (EETM), Fluid Kinetics Module (FKM), and Plasma Chemistry Monte Carlo Module (PCMCM) were employed. The EMM solves the frequency domain form of the wave equation for the inductively coupled fields. In the EETM, the electron Monte Carlo simulation provides electron energy distributions of bulk electrons. A separate Monte Carlo simulation is used for secondary, sheath accelerated electrons. The FKM solves heavy particle and electron continuity, momentum, energy

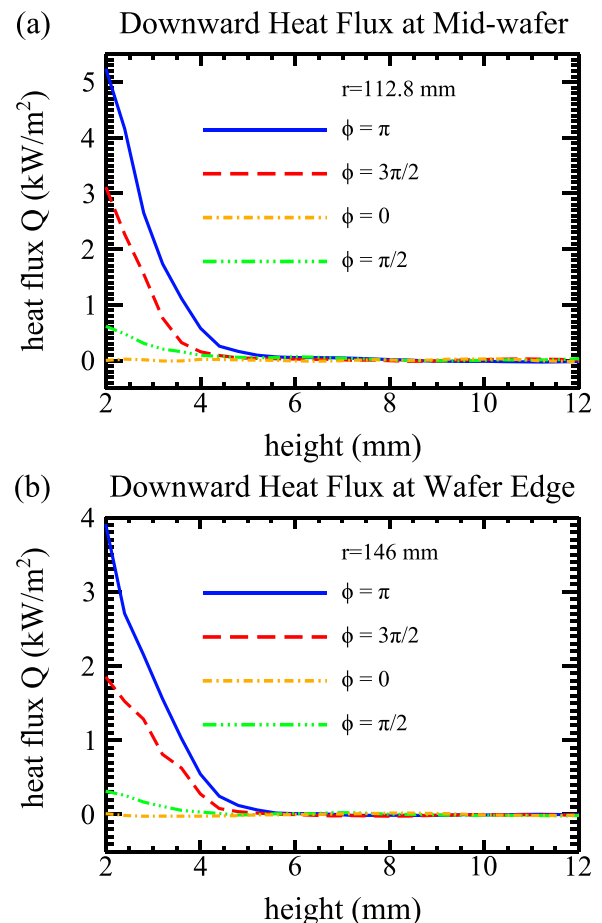


FIG. 12. Calculated downward heat flux at four different bias phases at two different radii: (a) $r = 112.8$ mm and (b) $r = 146$ mm.

and Poisson's equation for the electric potential. These three modules transfer parameters to the other modules using time-slicing techniques. When a quasi-steady state is reached, the PCMCM is used to obtain ion energy (or velocity) and angular distributions in the bulk plasma, pre-sheath, sheath and wafer. Pseudo-particles representing ions are launched from the site of their formation and their trajectories are integrated as function of time using electric fields from the FKM recorded as a function of phase. Collisions are accounted for using Monte Carlo techniques. As improvements to the previously described PCMCM, a finer sub-mesh is used within the HPEM in order to resolve ion transport from the bulk, through the presheath and sheath, and onto the wafer. Statistics on the velocity components of the ion trajectories are recorded as function of position (radius and height above the wafer) and phase during the rf cycle. The position of the sub-mesh was chosen to match with LIF measured area (100–148 mm in radius and 0.2 to 6 mm above the wafer).

The reactor for the simulation is essentially the same as in the experiment as shown in Fig. 1(a)—an inductively coupled plasma with a 2 MHz bias on the substrate. The gas pressure was 0.5 mTorr and gas mixture $\text{Ar}/\text{O}_2 = 80/20$ with a total flow rate of 50 sccm. The reaction mechanism for the Ar/O_2 plasma is discussed in Ref. 48. The ICP power deposition was 500 W and the substrate bias was 400 V. The

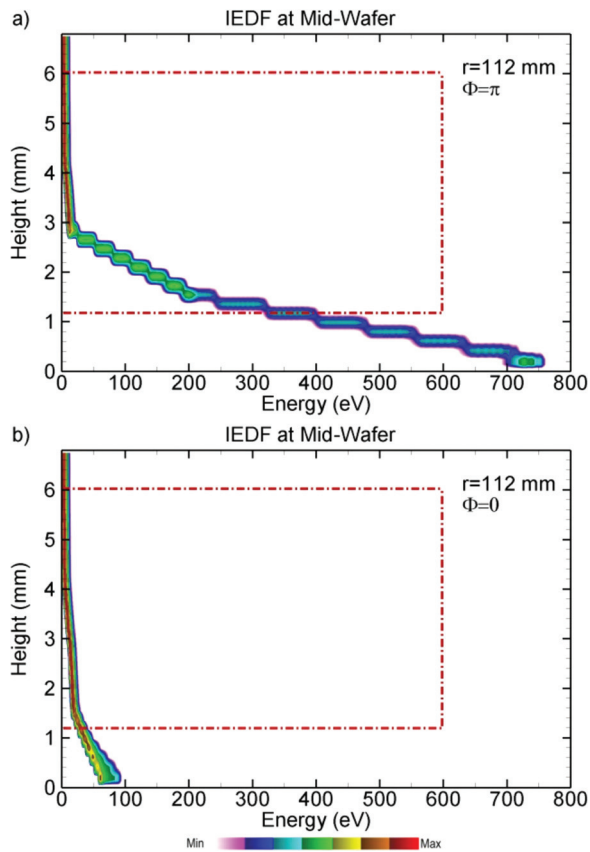


FIG. 13. Computed IEDs from bulk plasma through the sheath to the wafer at $r = 112$ mm for $\text{Ar}/\text{O}_2 = 80/20$, 0.5 mTorr for 2 MHz rf, 400 V amplitude and dc bias of -360 V. (a) Phase $\phi = \pi$ and (b) Phase $\phi = 0$. The stair-step appearance is due to the discreteness of the mesh upon which the IEDs are collected. The plot is in log scale.

self-generated dc bias is around -360 V. This voltage amplitude was chosen so that the predicted maximum energy of the IEDs within the spatial region accessible to measurements matched the experiments. (See discussion in Sec. V.) The sub-mesh resolution was 4 mm in radius and 0.4 mm in height. The phase resolution was 62.5 ns (8 phases within 2 MHz).

Predictions for the IEDs extend from the bulk plasma through the sheath to the wafer at phases of $\phi = \pi$ (most cathodic) and $\phi = 0$ (most anodic) are shown in Figs. 13 and 14 for an inner radius (112 mm) and at the wafer edge (148 mm). Comparing to the experimental results (Figs. 7 and 8), the model predicts a similar range of energies (350–400 eV) at 1.2 mm above the wafer at phase $\phi = \pi$. For the least negative bias, $\phi = 0$, the maximum energy is about 50 eV at 1.2 mm above and reach the wafer at 50–100 eV. The double-peaked nature of the IED begins at the sheath edge at about 4 mm. At this low frequency of 2 MHz, there is clear separation in phase of the low and high energy components of the IEDs regardless of radial position above the wafer. We have found that the details of IEDs near the edge of the wafer are sensitive to the charging of the focus ring, its dielectric constant and subtleties of its geometrical relationship to the edge of the wafer. The simulation predicts an edge effect of only 10 eV difference in the maximum of the IED since the sheath is fairly uniform in this reactor. The

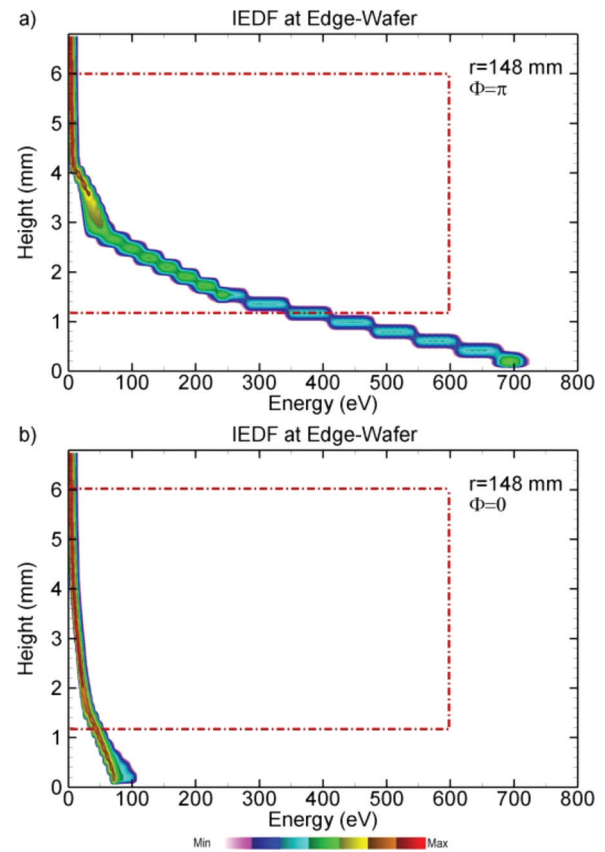


FIG. 14. Computed IEDs from bulk plasma through the sheath to the wafer at $r = 148$ mm for $\text{Ar}/\text{O}_2 = 80/20$, 0.5 mTorr for 2 MHz rf bias, 400 Volt amplitude and dc bias of -360 V. (a) Phase $\phi = \pi$ and (b) Phase $\phi = 0$. The stair-step appearance is due to the discreteness of the mesh upon which the IEDs are collected. The plot is in log scale.

experimental results (Figs. 7 and 8) confirmed this trend. The maximum energy at the surface of the wafer extends to 720–730 eV at the inner radius and 690–700 eV at the edge of the wafer, somewhat higher than that implied by experiments, 650 eV. Computed IEDs at a radius of 112 mm for a phase of $\phi = \pi$ at different heights above the wafer are shown in Fig. 15. For $\phi = \pi$ (most cathodic portion of the cycle), the low energy portion of the IED is nearly absent as the ions are essentially collisionlessly accelerated through the sheath. Comparison to the experimental results (see Fig. 5) confirms this separation in phase.

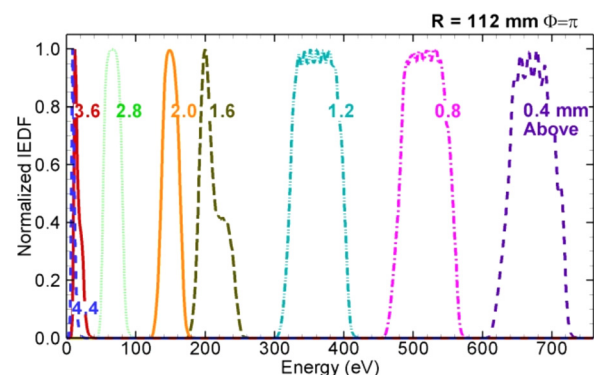


FIG. 15. Computed IEDs at a radius of 112 mm for a phase of $\phi = \pi$ for different heights above the wafer.

V. CONCLUDING REMARKS

Laser-induced fluorescence has been applied to measuring the perpendicular and parallel IVDs in the sheath above an rf-biased silicon wafer in a plasma etching reactor. The time-averaged energy distribution functions in transit through the sheath are generally not as sharply peaked as those arriving on the substrate which have been measured in several experiments^{20–27} or predicted by theory.^{9,14} These trends are consistent with previous measurements in this device.³⁴ Furthermore, the energy separations, ΔE_i , were less than values predicted by Panagopoulos:¹⁴ For $\omega_{rf}/\omega_{ion} = 0.3$ and a peak-to-peak sheath potential of 650 V, the predicted ΔE_i is 575 eV. Measured values in this experiment were approximately 220 eV at several spatial positions. Once again, this discrepancy has been seen previously in this machine and is most likely a result of the measurement height; it is not unreasonable to expect the ions to accelerate substantially over the remaining portion of the sheath, where the electric field is largest.

Illumination from a planar laser sheet allows simultaneous measurement of velocity distribution functions at multiple radial positions along the surface of the wafer. These measurements showed little variation in sheath thickness and maximum energy attained at the edge of the wafer as compared to values measured towards the middle of the wafer. Transverse velocity distribution function measurements show a lack of high energy ions, which reflect the small radial electric fields. Transverse drift of ions, however, do still contribute to net mean flows and heat flux. The contribution is most pronounced towards the edge of the wafer and the less negatively biased phases. This may help explain a relatively inferior etch quality for these regions of the wafer described in other tools.

Although there is good qualitative agreement between the model and the experiment, there is also a systematic difference as well. To obtain the same range of energies of IEDs and the same behavior of the IEDs as a function of phase within the spatial window that is accessible to the experiments, the amplitude of the rf voltage in the model must be larger than that in the experiment. These affects are on the order of 10%–20%. Many tests have been made of the model to confirm that all quantities are being correctly integrated, energy is conserved and theoretically derivable IEDs in idealized geometries can be reproduced. The key to these differences between the model and experiment is likely in the sheath structure 1 mm above the wafer that is not accessible to experiments and which is likely highly influenced by the details of the wafer charging, conductivity and dielectric constant of the wafer and stray capacitances of the wafer holder. Some aspects of these differences are likely a consequence of the discreteness with which Poisson's equation is solved in the plasma model. Although the total voltage drop across the sheath is not sensitive to this discreteness, the distribution of electric field within the sheath is sensitive. So it may be that ions are actually being accelerated less immediately adjacent to the wafer and more further from the wafer. Basic sheath theory would predict a different trend in which the electric field increases nearly linearly as one approaches

the wafer. However this basic theory was developed for cathode-fall like conditions with a fixed voltage on a metal electrode, and does not account for the details of surface charging and discharging as occurs on a mildly conducting wafer having a significant capacitive component to the current. For example, a larger negative charge on or near the wafer would reduce the electric field near the wafer and reduce the voltage drop across the sheath. An important finding of this work is that there are possible subtleties in the very near wafer region having to do with the details of wafer charging and capacitance that affect the sheath structure and in turn affect the development of IEDs as ions pass through the sheath.

ACKNOWLEDGMENTS

The experimental work was performed at UCLA Basic Plasma Science Facility. The experimental and computational work was supported by the National Science Foundation PHY-1004203. The computational work was additionally supported by the Department of Energy Office of Fusion Energy Science. The authors would like to thank Dr. Mike Barnes for his advice and guidance, and the Intevac Corp. for donation of the plasma etch tool.

- ¹M. A. Lieberman and A. J. Lichtenberg, in *Principles of Plasma Discharges and Materials Processing* (John Wiley & Sons, Hoboken, NJ, 2005).
- ²A. Metzke, D. W. Ernie, and H. J. Oskam, *J. Appl. Phys.* **60**, 3081 (1986).
- ³M. S. Barnes, J. C. Forster, and J. H. Keller, *IEEE Trans. Plasma Sci.* **19**, 240 (1991).
- ⁴D. B. Graves and M. J. Kushner, *J. Vac. Sci. Technol. A* **21**, S152 (2003).
- ⁵V. Georgieva, A. Bogaerts, and R. Gijbels, *Phys. Rev. E* **69**, 026406 (2004).
- ⁶J. K. Lee, O. V. Manuilenko, N. Y. Babaeva, H. C. Kim, and J. W. Shon, *Plasma Sources Sci. Technol.* **14**, 89 (2005).
- ⁷Z. Q. Guan, Z. L. Dai, and Y. N. Wang, *Phys. Plasmas* **12**, 123502 (2005).
- ⁸A. Agarwal and M. J. Kushner, *J. Vac. Sci. Technol. A* **23**, 1440 (2005).
- ⁹A. Agarwal, P. J. Stout, S. Banna, S. Rauf, K. Tokashiki, J.-Y. Lee, and K. Collins, *J. Appl. Phys.* **106**, 103305 (2009).
- ¹⁰P. Benoit-Cattin and L.-C. Bernard, *J. Appl. Phys.* **39**, 5723 (1968).
- ¹¹M. A. Liebermann, *IEEE Trans. Plasma Sci.* **16**, 638 (1988).
- ¹²P. A. Miller and M. E. Riley, *J. Appl. Phys.* **82**, 3689 (1997).
- ¹³E. Kawamura, V. Vahedi, M. A. Lieberman, and C. K. Birdsall, *Plasma Sources Sci. Technol.* **8**, R45 (1999).
- ¹⁴T. Panagopoulos and D. J. Economou, *J. Appl. Phys.* **85**, 3435 (1999).
- ¹⁵D. Bose, T. R. Govindan, and M. Meyyappan, *J. Appl. Phys.* **87**, 7176 (2000).
- ¹⁶J. Robiche, P. C. Boyle, M. M. Turner, and A. R. Ellingboe, *J. Phys. D* **36**, 1810 (2003).
- ¹⁷A. C. F. Wu, M. A. Lieberman, and J. P. Verboncoeur, *J. Appl. Phys.* **101**, 056105 (2007).
- ¹⁸J. P. Booth, G. Curley, D. Marić, and P. Chabert, *Plasma Sources Sci. Technol.* **19**, 015005 (2010).
- ¹⁹H. Shin, W. Zhu, L. Xu, V. M. Donnelly, and D. J. Economou, *Plasma Sources Sci. Technol.* **20**, 055001 (2011).
- ²⁰J. W. Coburn and E. Kay, *J. Appl. Phys.* **43**, 4965 (1972).
- ²¹K. Kohler, D. E. Horne, and J. W. Coburn, *J. Appl. Phys.* **58**, 3350 (1985).
- ²²A. D. Kuypers and H. J. Hopman, *J. Appl. Phys.* **67**, 1229 (1990).
- ²³A. Manenschijn, G. C. A. M. Janssen, E. van der Drift, and S. Radelaar, *J. Appl. Phys.* **69**, 1253 (1991).
- ²⁴M. A. Sobelevski, J. K. Olthoff, and Y. Wang, *J. Appl. Phys.* **85**, 3966 (1999).
- ²⁵M. A. Sobelevski, *J. Appl. Phys.* **95**, 4593 (2004).
- ²⁶J. R. Woodworth, M. E. Riley, P. A. Miller, G. A. Hebner, and T. W. Hamilton, *J. Appl. Phys.* **81**, 5950 (1997).

- ²⁷J. R. Woodworth, I. C. Abraham, M. E. Riley, P. A. Miller, T. W. Hamilton, B. P. Aragon, R. J. Shul, and C. G. Wilson, *J. Vac. Sci. Technol. A* **20**, 873 (2002).
- ²⁸N. Sadeghi, M. van de Griff, D. Vander, G. M. W. Kroesen, and F. J. de Hoog, *Appl. Phys. Lett.* **70**, 835 (1997).
- ²⁹L. Oksuz, M. Atta Khedr, and N. Hershkowitz, *Phys. Plasmas* **8**, 1729 (2001).
- ³⁰N. Claire, G. Bachet, U. Stroth, and F. Doveil, *Phys. Plasmas* **13**, 062103 (2006).
- ³¹B. Jacobs, W. Gekelman, P. Pribyl, M. Barnes, and M. Kilgore, *Appl. Phys. Lett.* **91**, 161505 (2007).
- ³²D. C. Zimmerman, R. McWilliams, and D. A. Edrich, *Plasma Sources Sci. Technol.* **14**, 581 (2005).
- ³³D. Lee, H. Hershkowitz, and G. Severn, *Phys. Plasmas* **15**, 083503 (2008).
- ³⁴B. Jacobs, W. Gekelman, P. Pribyl, and M. Barnes, *Phys. Rev. Lett.* **105**, 075001 (2010).
- ³⁵R. A. Stern and J. A. Johnson, *Phys. Rev. Lett.* **34**, 1548 (1975).
- ³⁶D. D. Burgess and C. H. Skinner, *J. Phys. B* **7**, L297 (1974).
- ³⁷D. N. Hill, S. Fornaca, and M. G. Wickham, *Rev. Sci. Instrum.* **54**, 309 (1983).
- ³⁸R. McWilliams, J. P. Booth, E. A. Hudson, J. Thomas, and D. Zimmerman, *Thin Solid Films* **515**, 4860 (2007).
- ³⁹M. J. Goeckner, J. Goree, and T. E. Sheridan, *Phys. Fluids B* **4**, 1663 (1992).
- ⁴⁰M. J. Goeckner and J. Goree, *J. Vac. Sci. Technol. A* **7**, 977 (1989).
- ⁴¹M. J. Goeckner, J. Goree, and T. E. Sheridan, *Phys. Fluids B* **3**, 2913 (1991).
- ⁴²S. Jun, H. Y. Chang, and R. McWilliams, *Phys. Plasmas* **13**, 052512 (2006).
- ⁴³E. V. Barnat and G. A. Hebner, *Appl. Phys. Lett.* **85**, 3393 (2004).
- ⁴⁴E. V. Barnat, P. A. Miller, G. A. Hebner, A. M. Paterson, T. Panagopoulos, E. Hammond, and J. Holland, *Plasma Sources Sci. Technol.* **16**, 330 (2007).
- ⁴⁵J. M. Hollis, J. E. Dorband, and F. Yusef-Zadeh, *Astrophys. J.* **386**, 293 (1992).
- ⁴⁶M. J. Kushner, *J. Phys. D* **42**, 194013 (2009).
- ⁴⁷J. Lu and M. J. Kushner, *J. Vac. Sci. Technol. A* **19**, 2652 (2001).
- ⁴⁸S. Rauf and M. J. Kushner, *J. Appl. Phys.* **82**, 2805 (1997).